1986

Wind-Driven Upwelling in the Vicinity of Cape Finisterre, Spain

Charles R. McClain

Shenn-Yu Chao

Larry P. Atkinson
Old Dominion University, laatkinso@odu.edu

Jack O. Blanton

Frederico De Castillejo

Original Publication Citation

McClain, C. R., Chao, S. Y., Atkinson, L. P., Blanton, J. O., & Decastillejo, F. (1986). Wind-driven upwelling in the vicinity of Cape Finisterre, Spain. *Journal of Geophysical Research: Oceans, 91*(C7), 8470-8486. doi:10.1029/JC091iC07p08470

JOURNAL OF GEOPHYSICAL RESEARCH, VOL. 91, NO. C7, PAGES 8470–8486, JULY 15, 1986

Wind-Driven Upwelling in the Vicinity of Cape Finisterre, Spain

CHARLES R. MCCLAIN,[1] SHENN-YU CHAO,[2] LARRY P. ATKINSON,[3] JACK O. BLANTON[4] AND FREDERICO DE CASTILLEJO[5]

Observations and numerical simulations of upwelling along the Galician coast of Spain during April 1982 are presented. In situ measurements include shipboard determinations of hydrographic and biological parameters from a grid of stations covering the continental shelf from Cape Finisterre to Ria de Vigo, sea level data from Vigo and La Coruña, and wind stress estimates derived from the ship winds and from surface pressure charts. Sea surface temperature information and pigment concentration information have been obtained from a sequence of satellite images from the NOAA 7 advanced very high resolution radiometer and the Nimbus 7 coastal zone color scanner, respectively. Since the Cape Finisterre sector of the Iberian peninsula is characterized by an abrupt change in coastline orientation, wind-driven upwelling can occur in that region over a 270° range of wind direction. These data document the evolution of upwelling and the resultant coastal circulation in response to two wind events that occurred over a 10-day period. Salient features of the circulation include a southward coastal jet and a northward flow further offshore along the western coast. Numerical simulations of the coastal currents, the vertical excursion of a density interface from a static equilibrium position, and coastal sea level are conducted using a wind patch characterized by constant direction and negative curl. The simulations show that during these wind events, the greatest upwelling will occur either at Cape Finisterre or along the northern coast as was observed in this case and as has been reported by others. It is suggested on the basis of the analysis of the sea level records and on the numerical simulations that wave disturbances propagate northward along the coast at a speed of 120–160 km/day. Finally, it is speculated that much of the organic material formed during upwelling events north of the Cape Finisterre is advected out to sea northwest of the cape.

INTRODUCTION

The western coast of the Iberian peninsula is the site of seasonal wind-driven upwelling from March through October [*Wooster et al.*, 1976]. This upwelling is part of a general system that extends southward to about 15°N. Along the Galician coast of Spain (Figure 1), the upwelling is most intense from April to August [*Fraga*, 1981] with the region between capes Finisterre and Ortegal exhibiting the coldest surface temperatures. During the remainder of the year, the winds are predominantly from the south, or downwelling favorable.

The irregular configuration of the Galician coastline and the general circulation of the offshore water masses add complexity to the response of the coastal waters to the wind. For instance, south of Cape Finisterre are five embayments, or rias, which cause enhancement of the upwelling through current-bathymetry interactions [*Blanton et al.*, 1984]. Also, the coastline abruptly ends its north-south orientation at Cape Finisterre and continues in an east-west direction east of Cape Ortegal. Thus upwelling favorable winds span a 270° range in direction in the immediate vicinity of Cape Finisterre. To complicate matters even more, the water masses along the western and northern coasts differ [*Fraga*, 1981; *Fraga et al.*, 1982]. The subsurface water mass (100–400 m) to the west of Galicia is North Atlantic Central Water (NACW), while the water to the north is a modified form of NACW. The former is distinguished by a nearly linear temperature-salinity T-S diagram having a slope of approximately 6°C per part per thousand. The northern water mass possesses a nearly constant salinity of 35.57 parts per thousand. These water masses intersect at Cape Finisterre and form a diffuse frontal zone which extends offshore toward the northwest.

The offshore subsurface circulation along the western coast is northward, but the surface flow is thought by some to be southward [*Fraga*, 1981]. Fraga's data were collected during the summer of 1976. On the other hand, northward surface currents in the upper 1500 m were reported by *Swallow et al.* [1977] for locations as close as 95 km from the coast during January and February 1977. The currents were determined from conductivity, temperature, and depth CTD casts and drifters and were of the order of 5 cm/s at the easternmost station. It is unclear why the two results differ, but they were derived from data collected during different seasons when wind conditions would have been dissimilar. *Blanton et al.* [1984] examined the western continental shelf circulation during April 1980 and found a nearshore subsurface flow to the south and a complex flow pattern at the surface which was generally northward. The apparent discrepancy between Fraga's interpretation and the findings of Blanton et al. was ascribed to the fact that April marks the transition between the seasonal downwelling and upwelling regimes. Another explanation could be that Fraga's survey did not sample the nearshore region with sufficient resolution to properly determine the circulation there. As we shall see later, winds during this transitional period are dominated by the passage of a series of eastward propagating cold fronts that generate complex circulation patterns. Finally, the general circulation along the northern coast is to the west, resulting in a convergence with the northward transport along the western coast, the convergence zone being the Cape Finisterre front mentioned earlier.

The coastal circulation in this region is of particular interest because Ria de Arosa and Ria de Muros are sites of commercial raft cultures of mussels [*Tenore et al.*, 1982] and the

[1] Laboratory for Oceans, NASA Goddard Space Flight Center, Greenbelt, Maryland.
[2] Center for Environmental and Estuarine Studies, University of Maryland, Cambridge.
[3] Department of Oceanography, Old Dominion University, Norfolk, Virginia.
[4] Skidaway Institute of Oceanography, Savannah, Georgia.
[5] Instituto Espanõl de Oceanografía, Málaga, Spain.

Paper number 6C0169.
0148-0227/86/006C-0169$05.00

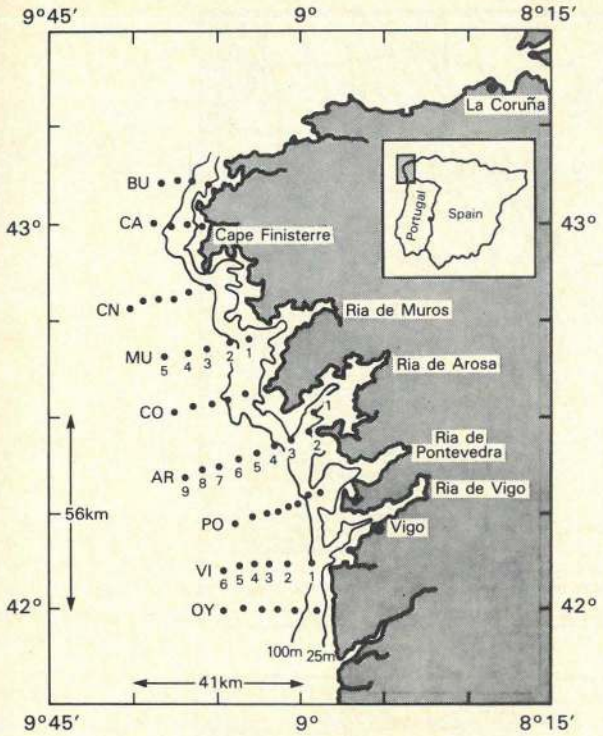

Fig. 1. Galician coast with 25-m and 100-m isobaths and the ship survey stations during the period of April 18–25, 1982.

narrow continental shelf serves as a nursery for hake. The two ecosystems are interdependent in that coastal upwelling provides the nutrient source for the raft cultures, which in turn generate substantial quantities of detritus. The detritus is thought be transported out of the rias in a bottom boundary layer and deposited on the shelf, where it supports a sizable benthic community [*Tenore et al.*, 1984]. Freshwater runoff into the rias is not a major source of nutrients, but it does significantly alter the water mass adjacent to the rias. It is believed that the sizable interannual variability in shellfish production is linked to a corresponding variability in the cumulative strength of the upwelling during the upwelling season.

In this report we present a case study of two consecutive upwelling events which occurred in April 1982. We have examined the available data regarding the prevailing wind conditions and sea level records for the entire month, hydrographic observations made during the period of April 18 to 26 and on April 29, and satellite imagery of sea surface temperature and pigment concentration spanning April 13 to 29. The sea level data were collected at Vigo and La Coruña on the western and northern coasts, respectively. During the survey, a cold front passed through the study area, which produced a major upwelling resulting in considerable increases in the pigment concentrations north of Cape Finisterre and within the rias. This data set is used to support a conceptual model of the circulation along the NW Spanish coast during the upwelling season. It is felt that the scenario described in this work is typical of this region and that events of this nature are primarily responsible for much of the region's productivity.

The Winds

Surface pressure charts reveal that the wind stress field for April was dominated by a series of eastward propagating cold fronts. Figure 2 traces the evolution of a typical cold front on April 19. This front originated far offshore, being west of 40°W prior to April 16. Long before the arrival of the cold front, winds in the vicinity of the Spanish coast were weakly southwestward. As the front approached the coastline, the southwestward winds strengthened over the coastal ocean (Figures 2*a*–2*c*), and after the front passed, the coastal winds quickly relaxed and shifted to a more westward direction. Typical translational speeds of these cold fronts range from 600 to 1000 km/day. Moreover, this weather pattern repeated itself every 10 days or so. Our satellite images and in situ measurements suggest that the circulation along the northwestern coast of Spain is dominated by these events.

In order to get a clearer idea about the local wind patterns, we have combined information on the wind stress as derived from surface pressure charts (Figure 3*a*) and ship observations (Figures 3*b* and 3*c*). No other meteorological data were available and the data in Figure 3*a* was provided by the Instituto Español de Oceanografía. The estimates in Figure 3*a* correspond to a point 150 km west of Cape Finisterre and were computed in the same manner as was described by *Blanton et al.* [1984]. The procedure simply takes the geostrophic wind as derived from the pressure chart, multiplies that value by 0.7, and cyclonically rotates the vector by 15° to estimate the surface wind velocity. A square law was used with a drag coefficient of 2.0×10^{-3} to transform velocity to stress. For the sake of consistency, the ship winds were similarly converted to stress, but with no correction made for the anemometer height or hull effects. The ship data were divided into offshore observations (Figure 3*b*), which averaged roughly 20 km from the coast, and observations at the mouth of Ria de Arosa from stations AR 1 to AR 3 (Figure 3*c*). The offshore vectors in Figure 3*b* are averages of representative measurements obtained during intervals of approximately 6 hours. The mean number of samples per interval was four and ranged from two to six. While these data are crude, when combined they do contain most of the essential features of the prevailing winds during and after the passage of the front.

Upon examination of Figure 3, several dissimilarities in the winds at the three locations are apparent. For instance, the Arosa winds were consistently strong with a heading to the southwest, parallel to the axis of the ria, while a small distance offshore the winds were generally much weaker, except on April 19 when an event occurred. It is clear that orographic effects were playing an important role in the coastal meteorology. The event on April 19 was observed while the Butria (BU) transect was being made and the winds reached 15 m/s. The orientation of the wind vector off Cape Finisterre at that time was parallel to the section of coast between capes Finisterre and Ortegal. The pressure chart analysis does not indicate an event until April 24. After the front's passage the Arosa winds remained strong, but the offshore winds essentially vanished. Thus the ship data indicate the existence of a large negative wind stress curl. Although the large-scale pressure charts indicate a negative curl associated with the cold front, they do not reveal this intense small-scale feature. On April 20 the southward component of the wind stress was about -2 dyn/cm^2 at Arosa but was zero 20 km offshore, so the wind stress curl was of the order of -0.1 dyn/cm^2/km.

Hyrographic Observations

Shipboard measurements were made from the *Garcia del Cid*, and the station grid is shown in Figure 1. The Arosa transect was occupied four times and represents a time series

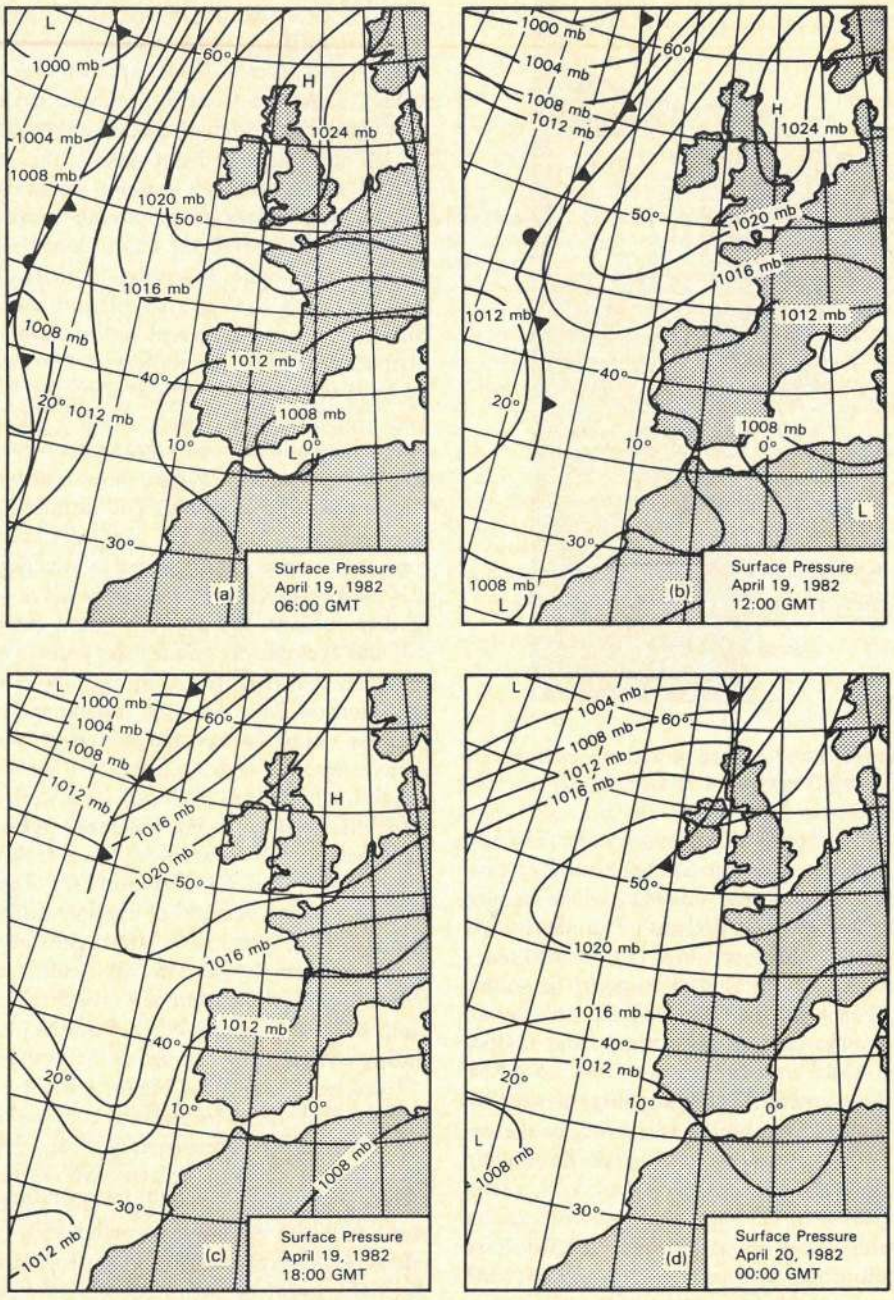

Fig. 2. Surface pressure charts at (*a*) 0600 UT, (*b*) 1200 UT, and (*c*) 18:00 on April 19 and (*d*) 0000 UT on April 20.

of events (station AR 3 was sampled six times), while the remaining sections were surveyed only once. Water samples were obtained using Nansen bottles, and temperature was measured with reversing thermometers. Salinity, nutrients, oxygen, chlorophyll *a* and phaeophytin concentrations were determined using standard techniques. Occasionally, temperature profiles were made with expendable bathythermographs.

In order to obtain a picture of the alongshore structure in the density field, the transects off Muros (MU), Arosa, and Vigo (VI) are shown in Figure 4. The Butria and Castro (CA) transects were very short, so neither was included. The downwelling of isopycnals at the nearshore stations of the Muros and Vigo sections is presumed to be due to freshwater discharge from the rias. If this feature is ignored, all sections show upwelling within 20 km of the coast, accompanied by a downwelling further offshore. These transects indicate a southward flowing offshore coastal jet adjacent to a northward flowing offshore current.

The vertical similarity of the density field in each transect implies that the alongshore current was vertically coherent and suggests that the alongshore flow varied more or less linearly with depth. Assuming that alongshore currents vanished at the bottom, one can estimate the current shear from the slopes of isopycnals. If the thermal wind relationship is invoked, the vertically averaged alongshore current is approximated by

$$V \approx \frac{g}{2f\rho_0} \int \frac{\partial \rho}{\partial x}\, dz \qquad (1)$$

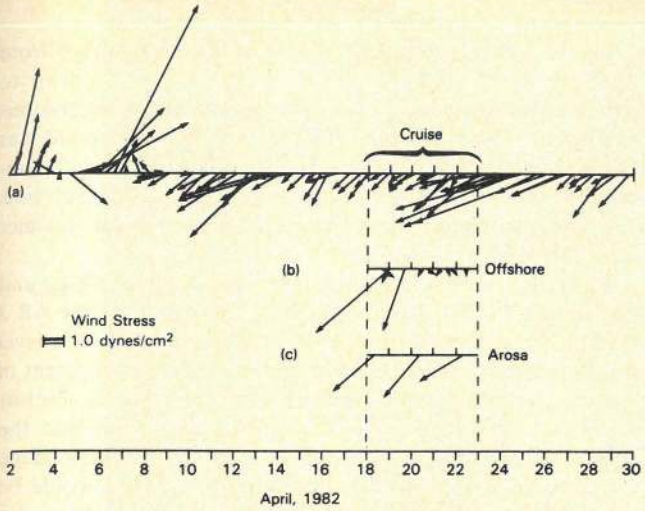

Fig. 3. Wind stress estimates from surface pressure charts and the ship. Winds from the surface charts (Figure 3*a*) corresponds to a point 150 km offshore of Cape Finisterre. The ship winds are separated into averages of observations within 6-hour periods for offshore stations (Figure 3*b*) and stations AR 1–AR 3 near the mouth of Ria de Arosa (Figure 3*c*).

where the integration is from the bottom to the surface and all other variables have their conventional meanings. Taking $\partial\rho/\partial x = 2 \times 10^{-10}$ g/cm^4 and the ocean depth H as 150 m, V is of the order of -15 cm/s. Thus the average alongshore flow

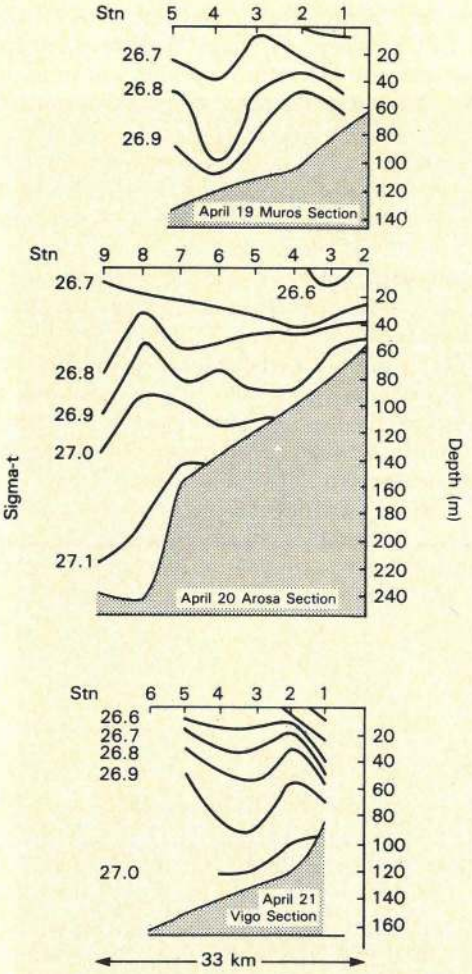

Fig. 4. Vertical density field from the Muros (MU), Arosa (AR), and Vigo (VI) transects.

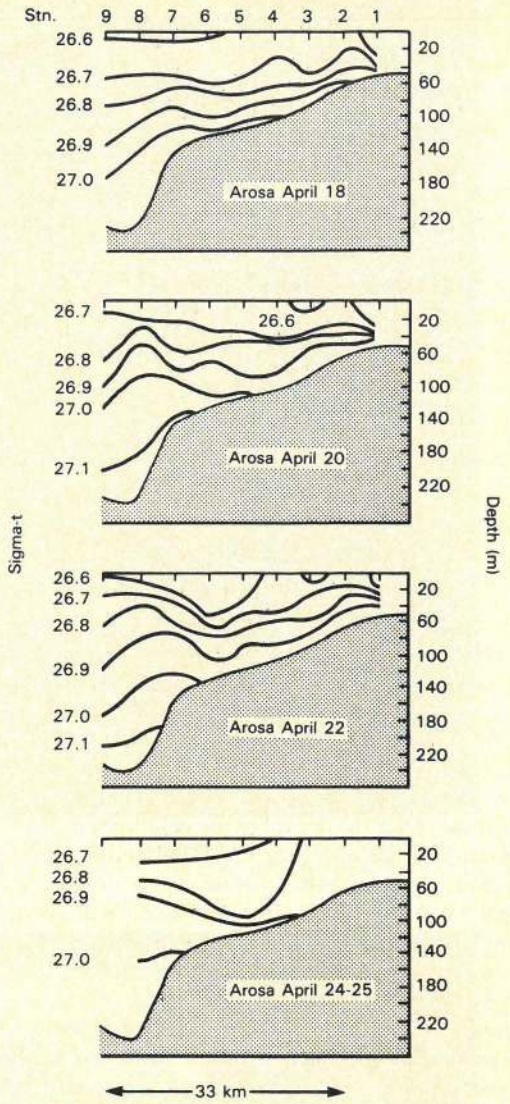

Fig. 5. Time series of four density sections from the Arosa transect. The transects were made on April 18, 20, 22, and 24–25.

has maximum southward speed of about 15 cm/s. Proceding westward, the isopycnals upwell with a similar but negative slope, indicating that the northward current had about the same speed.. The distance between the two maxima was around 20 km, so the vorticity of these currents was of the order of -1.5×10^{-5}/s.

If the horizontal current shear was driven by the negative wind stress curl associated with the cold front, then, assuming $\partial/\partial y \approx 0$,

$$r_b \frac{\partial V}{\partial x} \approx \frac{1}{\rho} \frac{\partial \tau}{\partial x} \tag{2}$$

where τ is the wind stress. Thus the bottom friction r_b would be 0.067 cm/s, a value consistent with the commonly accepted bottom friction for coastal waters of 150-m depth. The *e*-folding time scale for the development and dissipation of this current shear, H/r_b, would have equalled 2.6 days. The above estimates are necessarily rough because of the lack of direct current measurements, but as will be shown later, they seem accurate enough to account for most of the observed features identified so far. It is therefore quite plausible to argue that the observed current shear was driven by the negative wind stress curl.

Figure 5 depicts the four Arosa density sections for April 18,

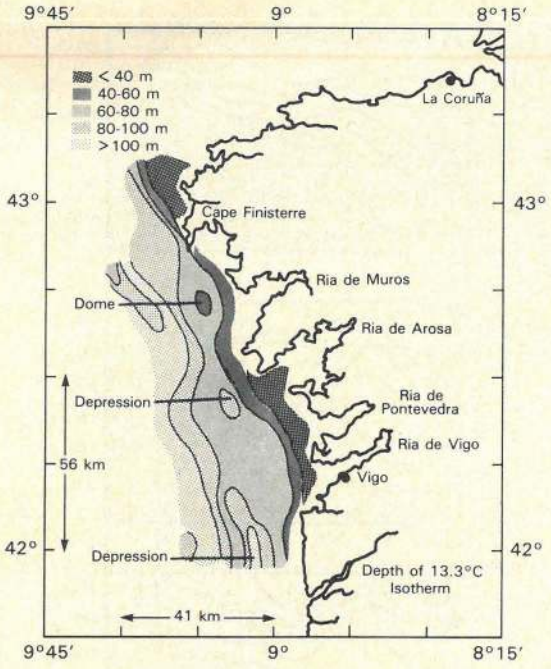

Fig. 6. Horizontal map of the depth of the 13.3°C isotherm from April 18 to April 21. Increments of 20 m are used.

20, 22, and 24–25, showing the temporal variability of the system. The Arosa section best illustrates the evolution of the density field. After the arrival of the cold front on April 19, the 26.8 σ_t surface, for instance, was continuously being elevated shoreward of station AR 4, while it was deepening between stations AR 4 and AR 5. This sequence illustrates the development of the southward flowing coastal jet and the northward current offshore, and it implies an *e*-folding time scale of about 3 days.

Figure 6 depicts the composite surface of the 13.3°C isotherm with 20-m contour intervals developed from stations occupied between April 18 and 21. The most pronounced upwellings occurred to the south of prominent offshore excursions in the 100-m isobath (see Figure 1) near rias de Muros and Pontevedra and resemble the upwelling reported by *Blanton et al.* [1984]. The gradual deepening of the isotherm in the offshore direction was not continuous in the alongshore direction, but instead, the density surface possessed a considerable amount of relief. Note the localized depressions near the mouth of Arosa and to the south of Vigo. The existence of this topography may have been due to coastline irregularities, but also, the 4-day time lag between the BU and OY sections probably resulted in some aliasing of transient events forced by the atmospheric frontal system.

The Sea Level

Figure 7 shows the hourly record of sea level at Vigo from April 15 to 29 during a period of transition from neap to spring tides. The vertical lines indicate the time of the Nimbus overpasses. The maximum tidal range during this period was about 3 m, which may influence the derived pigment concentrations in the shallow portions of the rias during ebb tide. The satellite images from the coastal zone color scanner (CZCS) will be discussed later.

Figure 8 provides 25-hour averages of sea level at Vigo and La Coruña and the depth of the 13.3°C isotherm for the AR 3 station. The arrival of the cold front induced a sharp sea level drop from April 18 to 21, again indicating the development of the southward flowing coastal jet. The postfront sea level at Vigo rose slowly from April 21 to 26, suggesting that the coastal jet was relaxing. Sea level at Vigo and the thermocline depth at AR 3 were more or less out of phase. This would be expected if the southward coastal jet satisfied the Margules equation. The sea level at La Coruña dropped continuously from April 19 to 26 and slowly relaxed thereafter. Consequently, the two sea level records have the visual appearance of being out of phase after the passage of the cold front. Why the sea level along the western and northern coasts shifted out of phase after the frontal passage will be addressed later using a conceptual model.

Satellite Images

The satellite data presented in this paper consist of four advanced very high resolution radiometer (AVHRR) images and five CZCS images. All images have been remapped to a common transverse Mercator projection and registered to the coastline. Sea surface temperature (SST) estimates were derived from NOAA 7 AVHRR-II data using the algorithm described by *Strong and McClain* [1984]. A total of 31 ship to satellite comparisons of SST from April 18, 19, and 20 yielded a mean difference (ship minus satellite) of 0.16°C and an rms difference of 0.31°C. Plates 1, 2, 3, and 4 illustrate the SST patterns on April 13, 18, 20, and 29, respectively. The image from April 19 is not presented, since it illustrates an intermediate stage between April 18 and 20 and provides no additional insights. Table 1 presents the color code for SST. All images before, during, and after the cold front passage show a marked temperature gradient near Cape Finisterre, the temperatures along the northern coast being considerably colder than those along the western coast. An examination of the SST fields on April 13 and 20 indicates that substantial warming had occurred along the western coast. However, on April 19 the SSTs north of Vigo began to drop. A comparison of SSTs on April 13 and 20 from 41°N to 44°N along the 9.5°W meridian

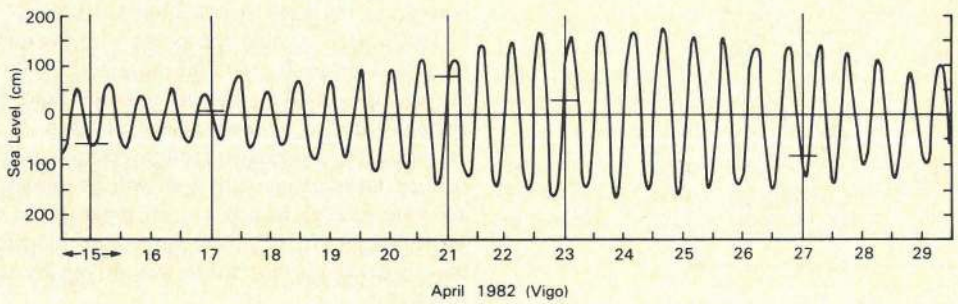

Fig. 7. Sea level at Vigo from April 15 to 29. The times of CZCS overflights are indicated by vertical lines.

Plate 1. AVHRR sea surface temperature image on April 13, 1982. All satellite images have been remapped to a common transverse Mercator projection having boundaries of 41.0°0-44.0°N and 7.5°–10.5°W and are registered to the coastline. Table 1 provides the color code.

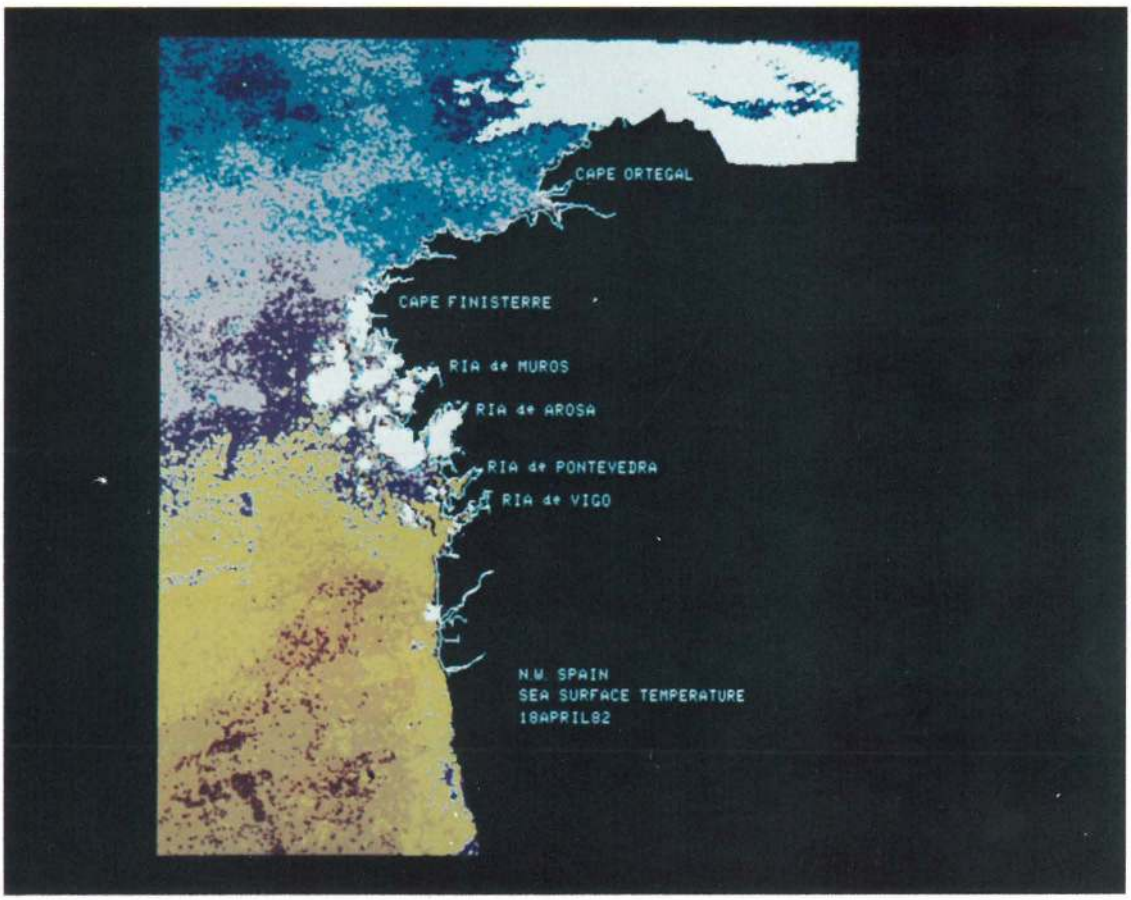

Plate 2. AVHRR sea surface temperature image on April 18, 1982.

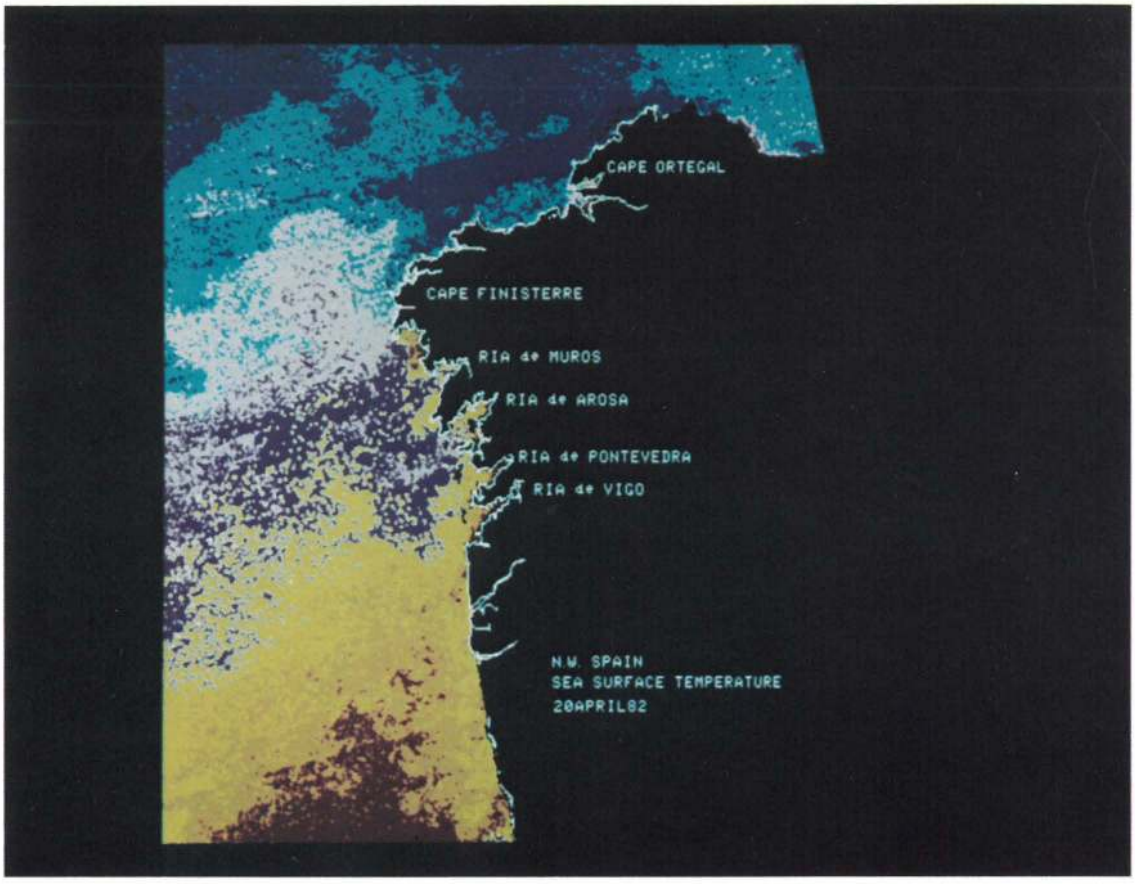

Plate 3. AVHRR sea surface temperature image on April 20, 1982. Note that the continental shelf surface water between Cape Ortegal and Vigo was cooler than it was on April 18.

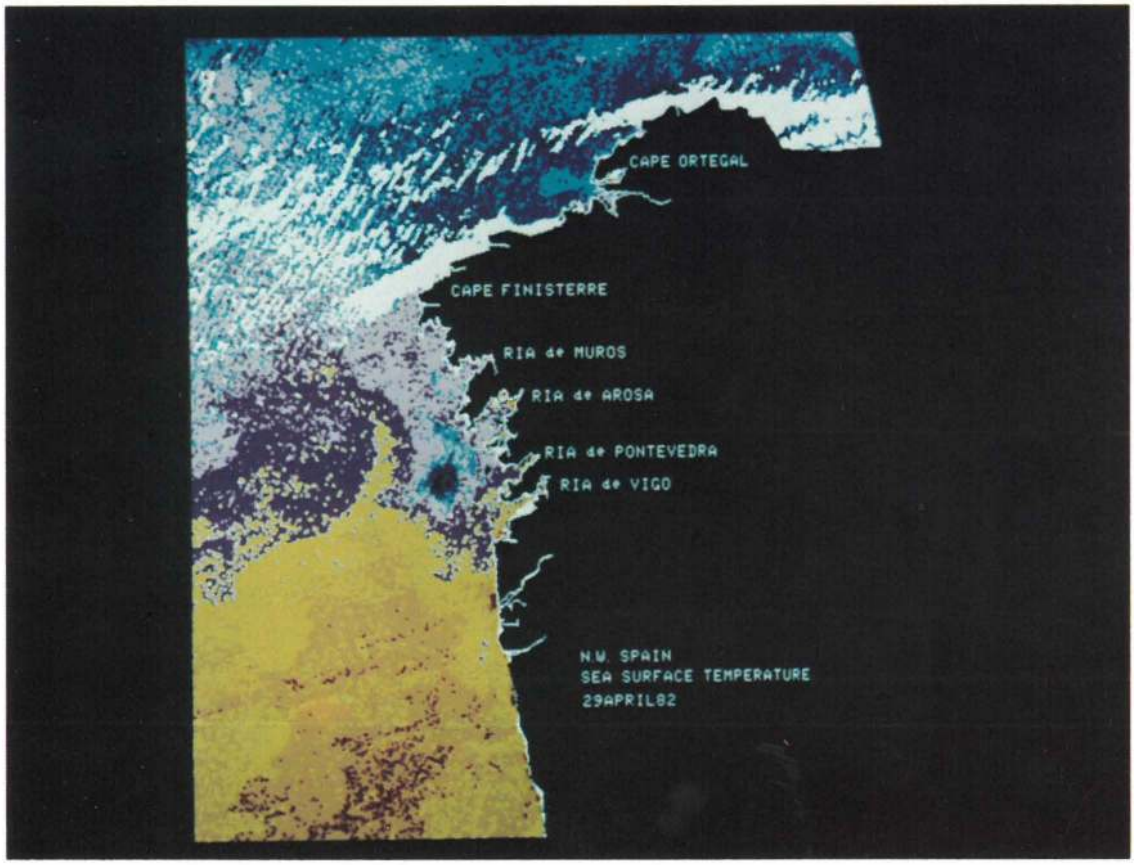

Plate 4. AVHRR sea surface temperature image on April 29, 1982.

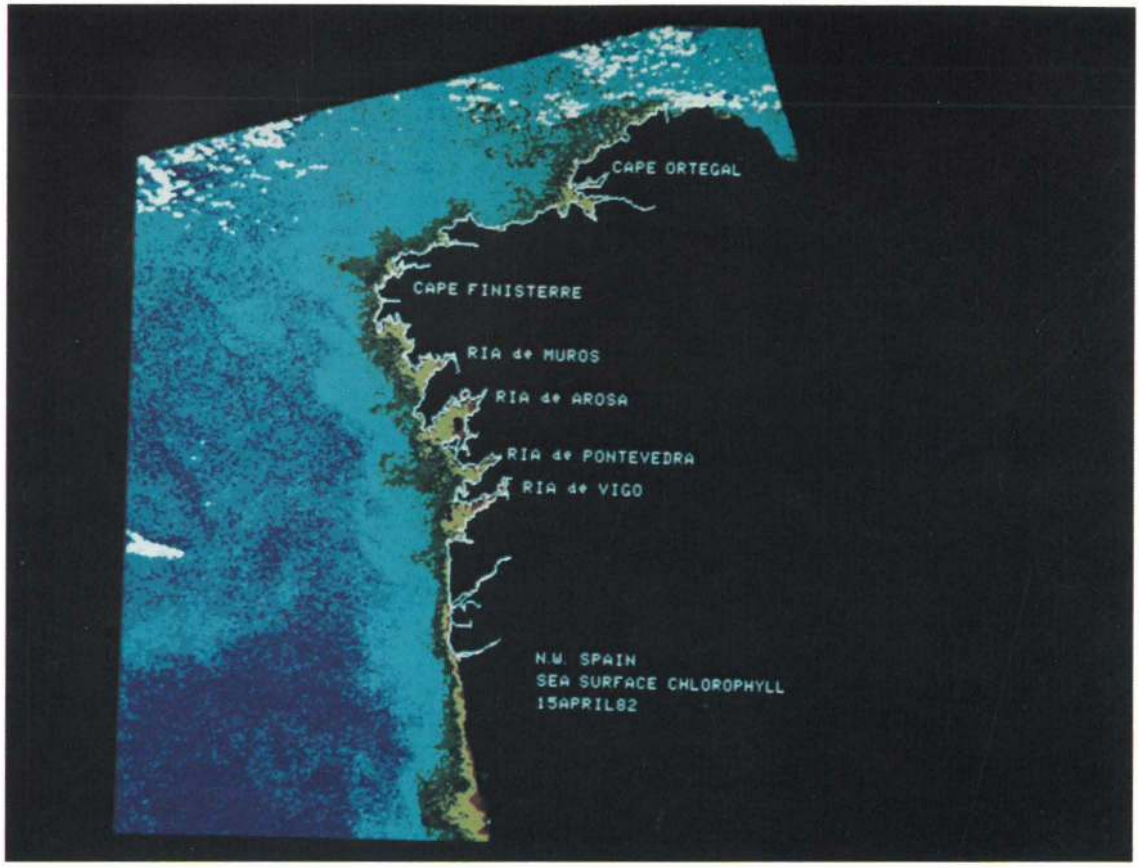

Plate 5. CZCS surface pigment concentration image on April 15, 1982. Pigment concentration is the sum of chlorophyll *a* and phaeophytin. The image was collected at low tide. Table 2 provides the color code. The Angstrom exponents used in the aerosol corrections of CZCS channels 1 to 3 are -0.36, -0.43, and -0.28, respectively.

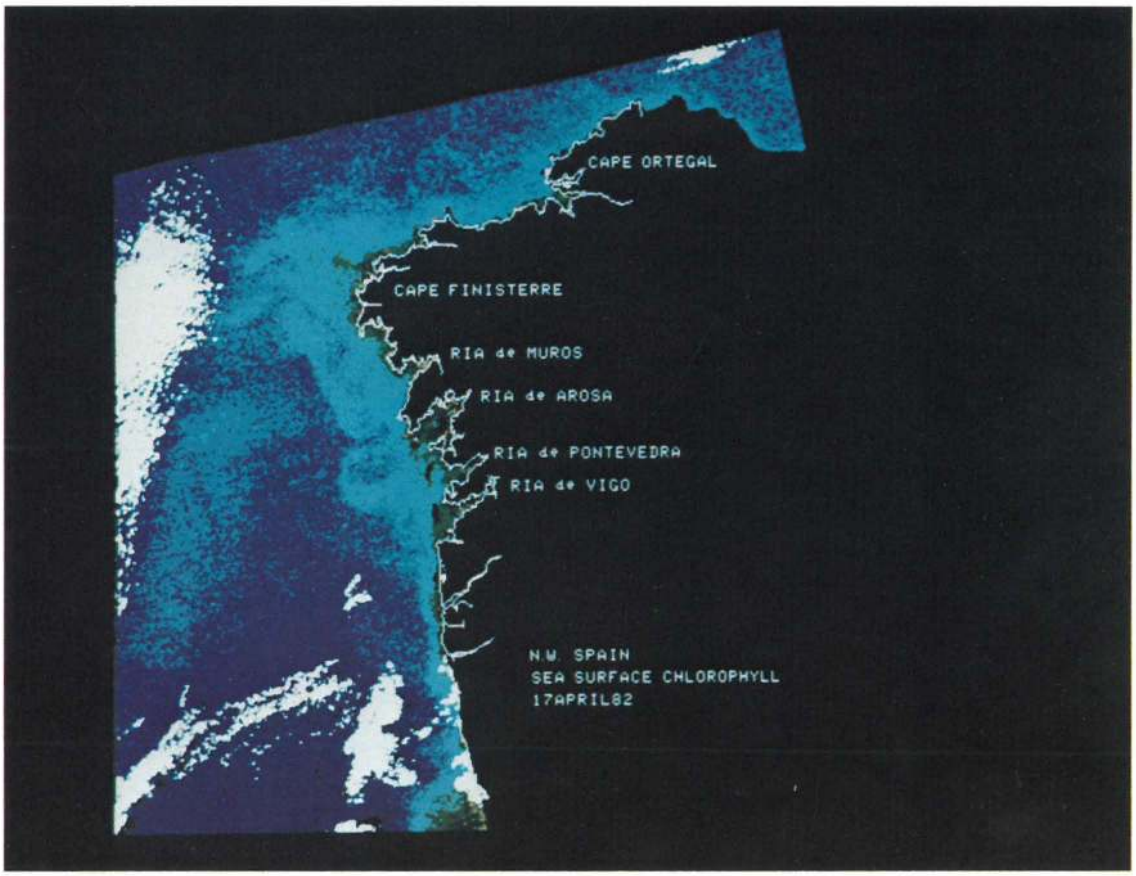

Plate 6. CZCS surface pigment concentration image on April 17, 1982. The image was collected during ebb tide. The Angstrom exponents are -0.17, -0.26, and -0.10.

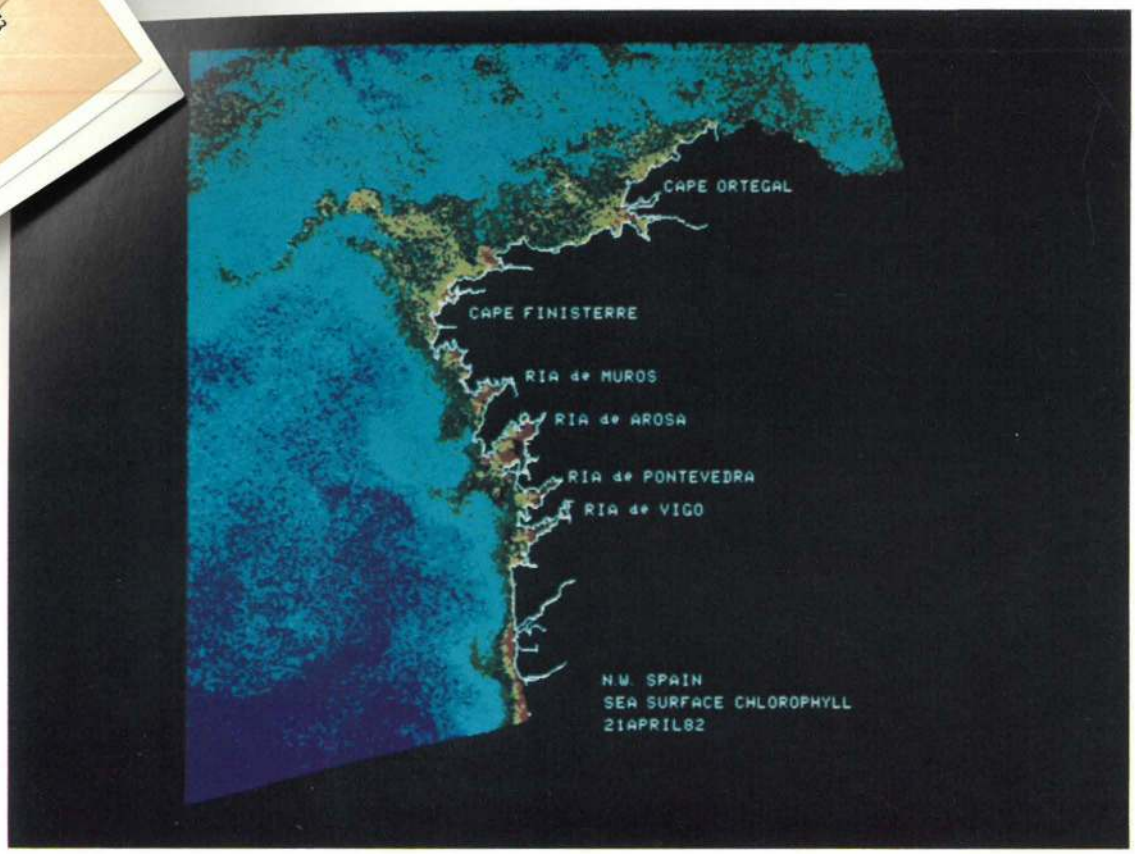

Plate 7. CZCS surface pigment concentration image on April 21, 1982. The image was collected near high tide. The Angstrom exponents are −0.36, −0.55, and −0.18.

Plate 8. CZCS surface pigment concentration image on April 23, 1982. The image was collected during flood tide near mean sea level. The Angstrom exponents are −0.28, −0.40, and −0.15.

Plate 9. CZCS surface pigment concentration image on April 27, 1982. The image was collected near low tide. The Angstrom exponents are −0.36, −0.55, and −0.18.

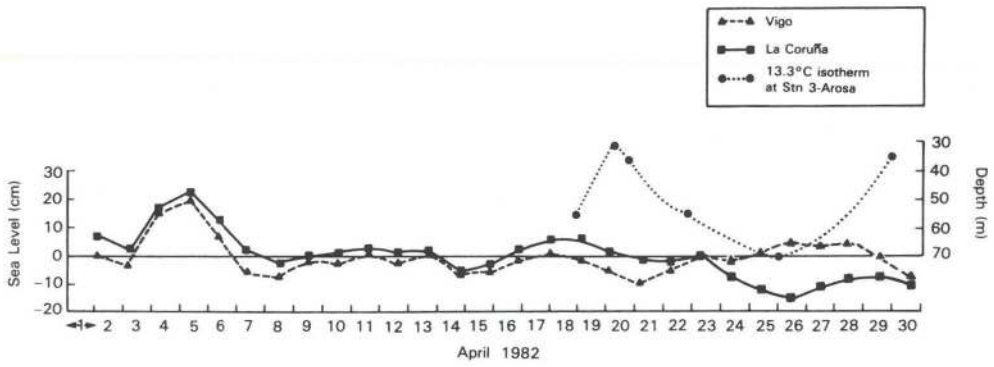

Fig. 8. Mean sea level (25-hour average) at Vigo and La Coruña and 13.3°C isotherm depth at station AR 3.

reveals that the temperature range had changed from (15.08°C, 12.72°C) to (15.97°C, 12.33°C) and that the mean alongshore temperature gradient remained nearly linear, increasing in magnitude from −0.008°C/km to −0.012°C/km. On April 20 the coastal surface waters between Cape Ortegal and Vigo were cooler than they were on April 18 and 19, and the mean SSTs between capes Finisterre and Ortegal on April 18, 19, and 20 were 12.97°C, 12.67°C, and 12.51°C, respectively. Also, from Plates 2, 3, and 4 the development of a narrow extrusion of warm water extending northward along the shelf break can be traced. This feature corresponds to features in the CZCS imagery and is due to the alongshore current patterns described earlier.

Plate 4 shows an intense localized area of upwelling off Ria de Arosa accompanied by colder water along the western coast than had been previously present. *Barbieri et al.* [1983] examined the radiances in the five radiometer channels and concluded that it was not an anamolous signature due to thin clouds or fog. The shoaling of the 13.3°C isotherm on April 29 (Figure 8) supports their conclusion. Finally, in all four SST scenes there was relatively cold water at the mouth of Ria de Arosa, a result that is consistent with Figure 6. Figure 3*a* shows a strong wind event passing through the area on April 24 and 25, but no ship wind data were collected after April 23.

Plates 5, 6, 7, 8, and 9 are CZCS images from April 15, 17, 21, 23, and 27, respectively. Table 2 provides the color convention for pigment concentration. From the CZCS data, surface pigment concentrations were derived by applying the "clear water radiance" atmospheric correction technique [*Gordon et al.*, 1983*a*] and using the calibration correction algorithm discussed by *Gordon et al.* [1983*b*]. Ship surface pigment observations on April 21 were collected at 16 stations along the three southernmost transects and span the period of 0700 to 2000 UT. The in situ values ranged from 0.03 to 0.32 mg/m^3 (mean = 0.14), while the CZCS (9-pixel average) yielded somewhat higher values ranging from 0.18 to 0.59 mg/m^3 (mean = 0.30). The comparison at the time of the satellite overpass is 0.11 (ship) and 0.22 (CZCS). However, this limited comparison hardly serves as an indicator of the overall accuracy of the satellite estimates on April 21, especially since the values are so small. A rigorous validation of the CZCS pigment estimates requires an entire complement of optical measurements coordinated with the satellite at a number of stations with careful analyses of the pigment samples. In this paper, temporal and spatial trends are the main concerns, and on the basis of the available field observations alone, these would be difficult to delineate. In order to compare trends in the satellite and ship data sets, the Arosa section is used. Table 3 lists the pigment concentrations from the satellite images and three of the Arosa transects. The satellite data indicate in all cases a decrease in concentration from the ria to the shelf break, while the ship data show no consistent pattern. The ship value at station AR 9 on April 18 looks unreasonably high, but values at 10 and 20 m were 0.76 and 0.53 mg/m^3, respectively. The ship data disclose that concentrations along the section dramatically increased between April 18 and 22 and that those values are consistent with the satellite values on April 17 and 21. The image on April 23 indicates a sharp decrease when compared with the data on April 21 and 22, and some feasible explanations are suggested below. Possible sources of error in the methodologies applied in obtaining and interpreting these estimates include sensor calibration, the aerosol corrections, the bio-optical algorithm, the analysis of the water samples, and aliasing of the field data due to the time

TABLE 1. Sea Surface Temperature Color Code

Color	Temperature, °C
Black	land
Dark blue	11.25–11.88
Blue	11.88–12.50
Light blue	12.50–13.13
Light purple	13.13–13.75
Purple	13.75–14.38
Yellow	14.38–15.00
Orange	15.00–15.63
Red	<15.63
White	clouds

TABLE 2. Sea Surface Pigment Concentration Color Code

Color	Concentration, mg/m^3
Black	land
Dark blue	0.08–0.17
Blue	0.17–0.25
Light blue	0.25–0.45
Light green	0.45–0.70
Dark green	0.70–1.00
Yellow	1.00–2.00
Orange	2.00–4.00
Brown	4.00–34.00
White	>34.00/clouds

TABLE 3. Pigment Concentrations Along the Arosa Transect

	Station									
	0	1	2	3	4	5	6	7	8	9
Date										
April 15	1.67	2.08	1.44	1.46	0.74	0.51	0.45	0.55	0.32	0.22
April 17	0.82	0.75	0.51	0.58	0.26	0.21	0.21	0.21	0.20	0.26
April 18	...	0.38	0.42	0.40	0.24	0.58	0.18	0.62	0.42	1.20
April 20	0.76	0.28	0.74	1.00	1.42	1.08	0.18	0.38	0.24	0.26
April 21	1.87	1.97	1.50	1.24	1.08	0.81	0.53	0.52	0.52	0.33
April 22	2.76	2.57	1.79	2.60	2.51	1.63	1.07	0.21	0.51	0.29
April 23	1.56	0.92	1.20	0.61	0.47	0.37	0.39	0.34	0.34	0.33
April 27	1.20	1.10	0.94	0.90	0.51	0.51	0.54	0.55	0.35	0.29
Depth, m	41	50	58	81	101	120	140	171	245	250

The locations of the stations are given in Figure 1, and station 0 is slightly northeast of station 1. The concentrations are mg/m^3. Data on April 15, 17, 21, 23, and 27 are from the CZCS, and those on April 18, 20, and 22 are from the ship. No pigment data were collected on April 24. The CZCS values are nine-pixel averages.

required to conduct the transects. The satellite data were processed in a consistent manner, and the same techniques have been applied in a number of other regions, yielding quite acceptable agreement with sea truth. Therefore the images are considered to be representative of the true conditions.

The imagery suggests considerable temporal and spatial variability in the surface concentrations, and a number of processes besides growth resulting from upwelling would have contributed to the variability. Settling during periods of wind relaxation could also have been an important factor, since the winds fluctuated greatly, especially offshore (Figure 3). Zooplankton grazing is another factor which cannot be quantified in this case. Also, the concentrations on the outer western shelf are clearly enhanced by the transport of organic material out of the rias. Typical phytoplankton growth rates are of the order of a doubling per day, and sinking rates can be several meters per day. The CZCS estimates an optically weighted concentration over the first penetration depth (the depth over which 90% of the upwelled surface irradiance originates), as was discussed by *Clark* [1981]. Since the penetration depth for blue light ranges from 0 to roughly 20 m for coastal waters, the concentrations derived from the CZCS are sensitive to transitions between quiescent conditions and periods of rapid growth and resuspension associated with wind events. The greatest rate of increase was about a factor of 2 between April 20 and 21 (Table 3), which falls within the range of possible values. On the other hand, the largest average decrease, roughly a factor of 2 or 3, occurred between April 22 and 23. During that time the offshore winds were nearly zero (Figure 3*b*), and in the offshore areas (stations AR 4 to AR 9) it is conceivable that during a 1-day period the material within the first penetration depth had settled to depths where its influence on the upwelled surface radiance was significantly reduced, resulting in substantially diminished estimates of surface concentration. *Walsh and Esaias* [1986] have documented fluctuations in CZCS concentrations of this magnitude resulting from settling and resuspension by wind events in the Middle Atlantic Bight, but no confirmation can be provided in this case.

In Figure 3*c* it is not apparent that the ria winds subsided as the offshore winds had done, and therefore settling and resuspension would not have been a major contributing factor to the concentration variability. The pigment concentrations within the rias do not correlate with tidal amplitude or phase but tend to be coupled with the hydrography of the adjacent shelf (see Table 4). For instance, the low concentrations in Plate 6 correspond to a period of minimal upwelling (Figure 8) and minimal tidal amplitude (Figure 7), while the high values in Plate 7 correspond to a period of enhanced upwelling and near-maximum tidal amplitude. However, the CZCS image on April 23 indicates much lower concentrations in the rias than were present on April 21 and 22, even though the tidal amplitude had increased. It is suggested that the decline in concentrations within the rias on April 23 was related to the fact that upwelling had subsided, as was observed at station AR 3. On April 27, (Plate 9) the concentrations within the rias had generally increased, coinciding with an enhancement in coastal upwelling while the tidal amplitude had remained relatively large. The upwelling that was occurring on April 27 is assumed to have been due to the second wind event, a conclusion corroborated by the SST and hydrographic data collected on April 29. The moderate concentrations in the rias

TABLE 4. Relative Influence of Tides and Coastal Hydrography on Pigment Concentrations in the Rias

		Pigment Concentration			
Date	Location	Rias	Northern Coast	Tidal Parameters	Isotherm Depth, m
April 13		...	...	flood	...
April 15	Muros	1.48		0.57	
	Arosa	1.79		−0.55	
	Pontevedra	1.56		ebb	...
	Vigo	2.09			
	Mean	1.73	0.44		
April 17	Muros	0.38		0.45	
	Arosa	0.72		0.10	...
	Pontevedra	0.55		ebb	
	Vigo	0.77			
	Mean	0.61	0.25		
April 18		...	...	ebb	55*
April 19		...	...	ebb	33*
April 20		...	...	ebb	36*
April 21	Muros	1.92		1.15	
	Arosa	2.96		0.77	46
	Pontevedra	1.85		flood	
	Vigo	1.99			
	Mean	2.18	1.08		
April 22		...	...	...	55*
April 23	Muros	0.77		1.61	
	Arosa	1.04		0.40	60
	Pontevedra	0.57		flood	
	Vigo	0.56			
	Mean	0.74	...		
April 25		...	...	...	70*
April 27	Muros	0.98		1.33	
	Arosa	1.05		−0.80	53
	Pontevedra	4.41		ebb	
	Vigo	2.48			
	Mean	2.23	0.65		
April 29		...	...	ebb	35*

Pigment concentrations are in milligrams per cubic meter and are the average of nine pixels located at the center of the mouth of each ria. Tidal amplitude and instantaneous elevation (meters) and the tidal phase (ebb or flood) at the time of the satellite overpass at Vigo are given in that order. For AVHRR overpasses, only the phase information is provided. The depth of the 13.3°C isotherm at station AR 3 is in meters (an asterisk implies an actual observation). The other isotherm depths are estimated using a linear interpolation. The total water depth at station AR 3 is 81 m. Also included are the mean concentrations for the northern coastal area between capes Finisterre and Ortegal.

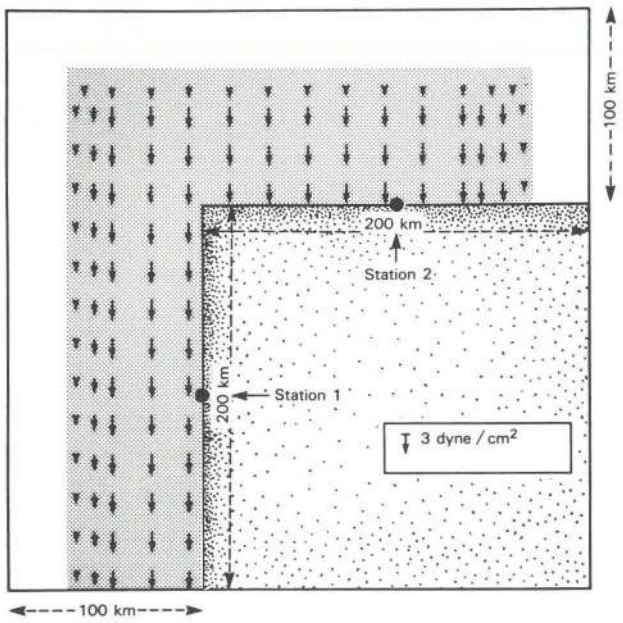

Fig. 9. Numerical model basin geometry and the definition of the southward wind field applied in the simulations. Stations 1 and 2 correspond to Vigo and La Coruña, respectively.

on April 15 (Plate 5) may have been the result of the earlier wind event on April 12 and 13 which caused a sea level drop beginning on April 13. Thus the CZCS images were collected at various times in the tidal cycle, but no striking correlation between concentration and tidal effects is apparent. These observations support the arguments that primary production within the rias is strongly influenced by coastal upwelling and that the tides simply serve as a mechanism for transporting the upwelled nutrients into the rias and for exporting organic material out of the rias and onto the shelf.

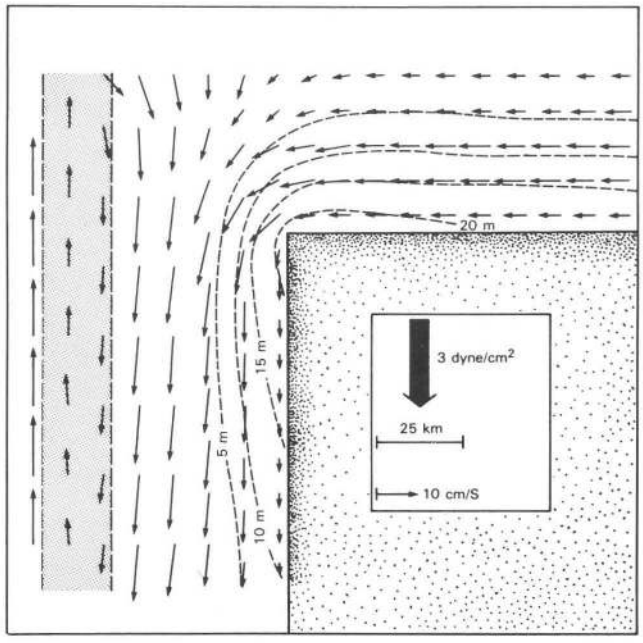

Fig. 10. The flow field and pycnocline displacement resulting from the wind field shown in Figure 9. Dashed lines are lines of constant displacement of the interface, and the shaded area defines the area of strong wind stress curl. The maximum wind stress is 3 dyn/cm^2.

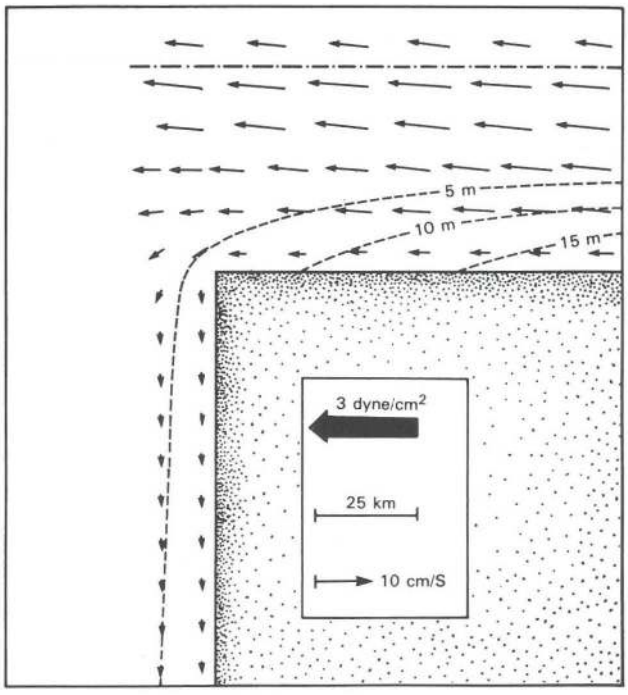

Fig. 11. The flow field and pycnocline displacement resulting from a westward wind configured with the northern coastline in an analogous fashion as in Figure 9.

The CZCS images provide a clear indication of the coastal circulation. Note that the plumes exiting from the rias consistently bend to the north at a distance of 20–25 km offshore. The rotation of the plumes toward the north is entirely consistent with the flow field discussed above. The plume emanating from Ria de Arosa on April 17 actually formed an eddy. The

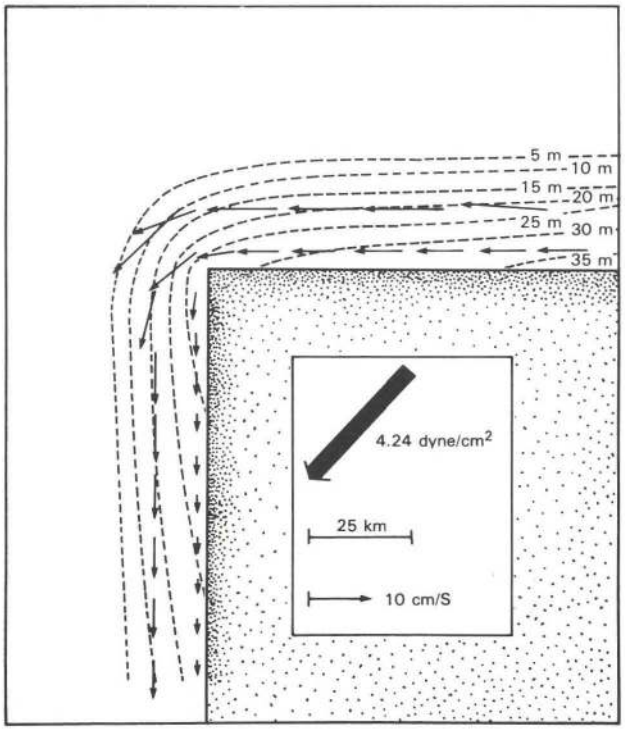

Fig. 12. The flow field and pycnocline displacement resulting from a wind to the southwest as determined by superpositioning the results shown in Figures 10 and 11. In this case the maximum wind stress is 4.24 dyn/cm^2.

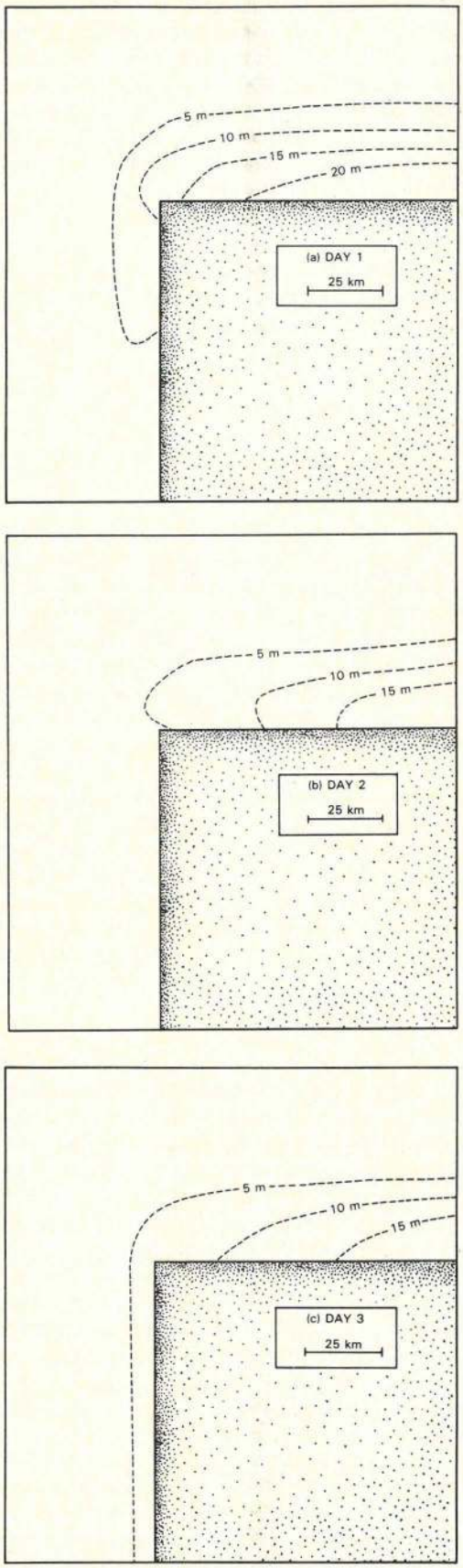

Fig. 13. The response of the pycnocline to a sudden wind shift from a southward to a westward direction. The initial flow conditions are those depicted in Figure 10. The shift occurs at time zero on the first day. The pycnocline elevation field is shown at the end of (*a*) 1, (*b*) 2, and (*c*) 3 days.

core of that eddy coincides with a depression in the 13.3°C isotherm shown in Figure 6.

The sequence of CZCS images illustrate the response of phytoplankton to the wind events on April 19 and 24. The image of April 17 indicates relatively low concentrations in the rias and to the north of Cape Finisterre prior to the first event. On April 21, soon after the frontal passage, a major phytoplankton bloom occurred. The bloom seems to have been centered near La Coruña coincident with the coldest coastal water (Plate 3) observed on April 21. Moreover, the width of the bloom along the northern coast was wider than it was along the western coast. Table 4 contains information on the mean concentrations between capes Finisterre and Ortegal and shows that the concentrations in the rias are correlated with those along the northern coast during this time. These features are consistent with the model results to be presented below. It is also apparent that much of the bloom was being transported offshore along the Cape Finisterre front which can be identified in Plates 3 and 7.

A Conceptual Model

In order to better clarify the wind-driven component of the coastal circulation corresponding to various wind fields, a simple numerical model has been developed. The simulations presented below are for winds from north, east, and northeast directions, each case resulting in quite different flow fields. In reality, the flow is more complex because of the large-scale circulation patterns in the Bay of Biscay and west of the Iberian peninsula upon which the local wind-driven flow is superimposed. Neither the large-scale circulation nor the Cape Finisterre front are taken into account, these considerations being beyond the scope of this study. Nonetheless, the model does succeed in reproducing the time-dependent phenomena discussed in preceding sections.

In a state of no motion, the model ocean consists of a thin upper layer with depth h and density ρ overlying a deep, inert lower layer with density $\rho + \Delta\rho$. Wind forcing is treated as a constant body force in the upper layer. Linear equations of motion, which describe the response of the baroclinic mode of the system, are

$$\frac{\partial u}{\partial t} - fv + \frac{1}{\rho}\frac{\partial p}{\partial x} = \frac{1}{\rho}\frac{\tau^x}{H} - r_i\frac{u}{H} + A_h\nabla^2 u$$

$$\frac{\partial v}{\partial t} + fu + \frac{1}{\rho}\frac{\partial p}{\partial y} = \frac{1}{\rho}\frac{\tau^y}{H} - r_i\frac{v}{H} + A_h\nabla^2 v \qquad (3)$$

$$\frac{1}{\rho}\frac{\partial p}{\partial t} + c^2\left(\frac{\partial u}{\partial x} + \frac{\partial v}{\partial y}\right) = -\frac{\sigma p}{\rho H}$$

The x axis is oriented eastward, the y axis is northward, and the z axis is upward. Velocities in the x and y directions are u and v, respectively, p is pressure, A_h is the coefficient of horizontal eddy viscosity, f is the Coriolis parameter, r_i is the friction coefficient at the density interface, σ is the Newtonian cooling coefficient [*Gill*, 1982], and c is a characteristic speed of the baroclinic model. The pressure field is related to the thickness of the upper layer, h, by

$$h = H + (p/g'\rho) \qquad (4)$$

where $g' = g\Delta\rho/\rho$ and g is the gravitational constant.

The model fixes six parameters throughout this study. They are $f = 10^{-4}$/s, $g' = 1$ cm/s^2, $H = 200$ m, $A_h = 2.5 \times 10^6$ cm^2/s, and $r_i = \sigma = 0.02$ m/s. Most of these choices are stan-

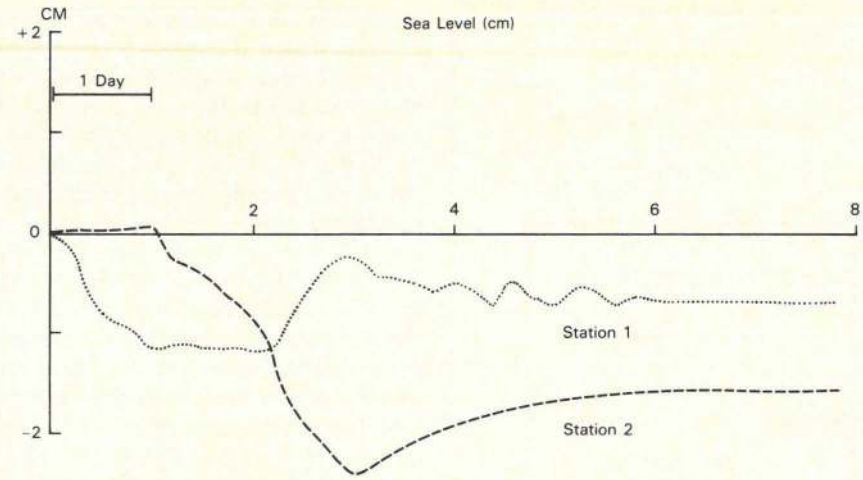

Fig. 14. Modeled sea level response at stations 1 and 2 as a result of the rapid shift from southward to westward winds. The model was spun up by applying the wind shown in Figure 9 for 2 days.

dard. The choice of g' and H yields a characteristic speed of gravity waves, $c = (g'H)^{1/2} = 1.41$ m/s, or equivalently, 120 km/day. This choice is somewhat arbitrary for lack of means to determine it a priori. The spin-up of the model ocean depends critically on the choice of c. A large value of c shortens the spin-up time, but a smaller c lengthens it. A comparison between the transient model response and the observed sea level fluctuations will help in estimating the speed of coastally trapped waves along the Iberian peninsula.

The ocean basin is shown in Figure 9, and no-slip conditions are applied at all boundaries. The model ocean is forced by a wind patch having the horizontal structure defined in Figure 9 for the case of a southward wind. In the following numerical experiments the wind direction will be changed, but the spatial structure of the wind remains fixed. The model wind patch does not extend over the whole basin in order to avoid the setup of a basin-wide pressure gradient force which tends to weaken the wind-driven currents. Also, a pronounced offshore wind curl was included in the wind patch for reasons discussed earlier. When the model wind is southward, there is a strong negative wind stress curl offshore of the western coast. If the wind is westward, the negative curl is present offshore of the northern coast. In order to dampen the recycling of Kelvin waves around the basin, the Newtonian cooling coefficient has been increased tenfold at grid points that are immediately adjacent to the northern and western boundaries. Although the model geometry and wind field are rather crude, the essential features of the coastal currents driven by the coastal wind and by the wind stress curl around a cape are delineated using this model.

Solutions to (3), subject to the boundary conditions, were obtained using the numerical scheme described by *Gent and Semtner* [1980], and the fields were evaluated on a staggered grid with a spacing of 5 km. The leapfrog method was used to advance the solution in time using a time step of 0.01 day. Typically, a 12-day integration was needed to attain an equilibrium state. Figure 10 shows the steady state circulation and the upward displacement of the interface around the cape driven by the southward wind stress field shown in Figure 9. The flow field is driven by two types of forcing, the direct action of the wind and the curl of the wind field. The nearshore current is primarily driven by the southward coastal wind along the western shoreline. The alongshore current immediately adjacent to the western coast increases poleward and reaches a maximum at the cape, while the nearshore flow along the northern coast is remotely forced by the western coastal wind and slowly decays eastward. Upwelling is most intense at the cape and decays both to the east and to the south. The width of the upwelling zone along the northern coast is considerably wider than that along the western coast. Offshore of the western coast, the flow field is primarily driven by the negative wind curl. The shaded area in Figure 10 identifies the region occupied by the strong wind shear. Currents forced by this wind field reach a maximum southward speed shoreward of the wind shear zone and a maximum northward speed offshore of the zone. Unlike the nearshore coastal jet, currents driven the by wind stress curl are locally forced and remain more or less uniform alongshore. Other simulations have shown that this is generally true even if the ocean stratification, the continental shelf and slope, and the beta effect are included.

Currents driven by a westward wind are quite different. If forced by a patch of alongshore wind, the strength of the coastal jet depends critically on the fetch length. Following the propagation direction of coastally trapped waves, the coastal jet is the weakest near the downwind edge of the wind patch, reaches a maximum near the upwind edge of the wind patch, and decays thereafter. The cross-shelf wind is ineffective in driving the alongshore jet and coastal upwelling along the western coast. For a southward wind, therefore, the coastal jet and upwelling are most intense near the cape. For the westward wind, however, the cape is at the downwind edge of the wind patch, and the coastal jet and upwelling are expected to be the weakest there. Figure 11 shows the flow field and upward displacement of the interface driven by the westward wind field. The cross-shelf wind along the western coast drives a negligible southward flow there. The coastal jet and the upwelling are the weakest at the cape and intensify eastward. Since the currents driven by the wind curl field are analogous to those in the previous situation, they are not discussed here.

The model ocean response to a southwestward wind can be obtained by a linear superposition of the last two results. Figure 12 shows the resultant flow field and interfacial displacement. The wind is upwelling favorable for both coasts, and the coastal jet strengthens continuously in the direction of Kelvin wave propagation. Upwelling is intense at the cape and

becomes even more intensified further eastward. The foregoing steady state calculations show that for an intense upwelling to occur near Cape Finisterre the upwelling favorable wind conditions must extend a considerable distance equatorward of the cape. This conclusion is consistent with our analyses of the wind field and the satellite images as discussed in the previous sections, and similar results have been obtained by *Hurlburt* [1974] and *Crepon et al.* [1984].

A sudden change of the wind field from a southward direction to a westward direction yields an interesting transient response. When the wind changes, the patch of the upwelling favorable wind is instantaneously displaced forward, so that the upwind edge of the wind band moves towards the cape. Figure 13 traces the evolution of the density interface after the wind rotation. In this experiment the flow field depicted by Figure 10 was used as the initial condition, and the wind field was switched impulsively to the westward direction. This situation simulates the two wind events discussed previously, where a wind event having a strong southward component was followed by a second event having a more westward orientation. The analogy is not perfect, since the observed wind events were separated by a finite period of slack winds and both wind events had southward components, but the observed SST fields follow a similar pattern. According to the model, the depth contours along the western coast respond quickly and move poleward at the speed of the Kelvin waves (120 km/day). Along the northern coast, the relaxation of the southward wind displaces the interface downward, while the onset of westward winds displaces it upward. The net result is a small and slow adjustment along the northern coast which takes about three days and quickly approaches equilibrium thereafter. Note that between days 1 and 2 (Figures 13*a* and 13*d*) the 5-m contour retreated northward around the cape, but by day 3 some upwelling was again occurring along the western coast. This is the result of local forcing by the offshore wind (see Figure 11).

Sea level data also reveal some important transient responses induced by the frontal passage. Prior to the arrival of the cold front, winds were weak and sea level fluctuations appear to have been locally forced. Consequently, sea level records at Vigo and La Coruña were nearly in phase. The arrival of the cold front induced a rapid setdown of sea level at Vigo, and a slow setdown at La Coruña. The beginning of sea level setdown at La Coruña lagged setdown at Vigo by 1 to 1.5 days. The postfront sea level at the La Coruña station relaxed more slowly beginning on April 22. Consequently, the two sea level records appear to have been shifted out of phase after the frontal passage.

The whole episode of the front's passage is crudely simulated as follows. The model ocean is assumed to be motionless before the front's arrival. The 2-day wind event during the frontal passage was simulated here by the sudden application of the southward wind field as shown in Figure 9. After 2 days the model wind field was switched westward, simulating the predominantly westward wind after the frontal passage. Pressure fields were recorded at two coastal stations. One was 100 km south of the cape and the other one was 100 km east of the cape representing the tide gage stations at Vigo and La Coruña, respectively. The locations of these two stations are marked in Figure 9. Sea level variations were computed from the pressure field using the hydrostatic relation. Figure 14 shows the adjustment of sea level at the two stations in response to the model wind event. Some of the features in the observed sea level records are reproduced here. The 2-day southward wind event forced a rapid setdown at station 1, but the sea level drop at station 2 did not begin until the arrival of the Kelvin waves and therefore involved a longer time scale. The sea level rise after the wind shift was rapid at station 1, but it was slower at station 2 and lagged the response at station 1 by approximately 1 day. All these features agree with observations, except for the magnitude of the sea level fluctuations. The difference between the observed and the modeled amplitudes stems from the fact that the model assumed a constant 200-m depth, while the tide gages were located in much shallower water. Also, the wind fetch affects the sea level variation. The meridional extent of the model wind field was considerably shorter than that of the observed wind field. Additionally, a significant portion of the sea level drop, remotely forced by the equatorward wind stress further to the south, is neglected by the model. In spite of these shortcomings, the model seems to be conceptually useful in that the salient features induced by the front's passage are qualitatively reproduced.

Conclusions

In the previous sections, we have merged various field and satellite data sets with a simple numerical model of the Galician continental shelf. Although some of the field data were not extensive, particularly the wind field, the data were sufficient to allow us to develop a consistent explanation for all of the observed phenomena. In particular, we have established that the upwelling along the Galician coast will be most prevalent along the northern coast regardless of whether the winds are from the east, northeast, or north. This situation has been consistently observed by ourselves and others. Winds from the southeast should favor upwelling along the northern coast, while winds from the northwest should drive upwelling primarily along the western coast; winds from the southwest should be downwelling favorable everywhere, although we do not treat these cases here. We have shown that the northward transport near the shelf break indicated in the CZCS imagery was the result of a negative wind stress curl in the immediate vicinity of the coast. The existence of the curl in the wind field was probably influenced by the adjacent coastal morphology in that the rias tended to channel the wind toward the southwest. This northward transport converges with the westward transport that exists along the northern coast for both southward and westward winds. This convergence occurs off Cape Finisterre and coincides with the front that demarcates the boundary of the two water masses found to the west and to the north of the Iberian peninsula. If this flow pattern is indeed typical of the upwelling season, then it is quite conceivable that much of the carbon fixed during these upwelling events is lost from the continental shelf as it is transported offshore along the Cape Finisterre front. Indeed, this conclusion is supported by Plates 7 and 9. The response time of the coastal circulation to wind forcing was found to be about 3 days. This result is supported by the satellite images, by the hydrographic sections along the AR transect, and by analytical and numerical computations. Since the system responds so quickly and relaxes somewhat more slowly, ship surveys must be planned so as to span at least one wind event cycle (about 10 days), and the region north of Cape Finisterre should be included in the survey. Another conclusion is that the sea level setdown at La Coruña lagged setdown at Vigo by about 1 day, suggesting that coastally trapped waves had a speed of

120–160 km/day. Finally, the data that have been presented indicate that the pigment concentrations within the rias are highly correlated with the intensity of upwelling occurring on the adjacent continental shelf and do not appear to be strongly influenced by tidal effects.

Acknowledgments. The authors would like to thank the Joint Committee of the U.S.-Spanish Treaty of Friendship and Cooperation, who partially funded this study, and Kenneth Tenore, who is the chief scientist. Additional support for this study was supplied by the Ocean Processes Branch at NASA headquarters. Our special appreciation is expressed to the Instituto Español de Oceanografia, with whom we have enjoyed working, and to F. Fraga for his cooperation. Also, we would like to recognize Judy Chen of the General Software Corporation in Lanham, Maryland, for her efforts in developing the image analysis software. Finally, we wish to thank the reviewers for their time and helpful comments.

References

Barbieri, R., C. McClain, and D. Endres, Methodology for interpretation of SST retrievals using the AVHRR split-window algorithm, *NASA Tech. Memo 85100*, 53 pp., 1983.

Blanton, J., L. Atkinson, F. de Castillejo, and A. Montero, Coastal upwelling off the Rias Bajas, Galicia, northwest Spain, I, Hydrographic studies, *Rapp. P. V. Reun. Cons. Int. Explor. Mer, 183*, 79-90, 1984.

Clark, D., Phytoplankton pigment algorithms for the Nimbus-7 CZCS, in *Oceanography From Space*, edited by J. F. R. Gower, pp. 227–237, Plenum, New York, 1981.

Crepon, M., C. Richez, and M. Chartier, Effects of coastline geometry on upwelling, *J. Phys. Oceanogr., 14*, 1365–1382, 1984.

Fraga, F., Upwelling off the Galician coast, northwest Spain, in *Coastal Upwelling, Coastal and Estuarine Sci.*, vol 1, edited by F. A. Richards, pp. 176–182, AGU, Washington, D. C., 1981.

Fraga, F., C. Mourino, and M. Manriquez, Las masas de agua en la costa de Galicia: Junio–Octubre, *Result. Exp. Cient., 10*, 51–77, 1982.

Gent, P., and A. Semtner, Jr., Energy trapping near the equator in a numerical ocean model, *J. Phys. Oceanogr., 10*(6), 823–842, 1980.

Gill, A., *Atmosphere-Ocean Dynamics*, 662 pp., Academic, Orlando, Fla., 1982.

Gordon, H., D. Clark, J. Brown, O. Brown, R. Evans, and W. Broenkow, Phytoplankton pigment concentrations in the Middle Atlantic Bight: Comparison of ship determinations and CZCS estimates, *Appl. Opt., 22*(1), 20–36, 1983*a*.

Gordon, H., J. Brown, O. Brown, R. Evans, and D. Clark, Nimbus-7 CZCS: Reduction of its radiometric sensitivity with time, *Appl. Opt., 22*(24), 3929–3931, 1983*b*.

Hurlburt, H., The influence of coastline geometry and bottom topography on the eastern ocean circulation, Ph.D. dissertation, 103 pp., Fla. State Univ., Tallahassee, 1974.

Strong, A., and P. McClain, Improved ocean surface temperatures from space—Comparisons with drifting buoys, *Bull. Am. Meteorol. Soc., 65*(2), 138–142, 1984.

Swallow, J., W. Gould, and P. Saunders, Evidence for a poleward eastern boundary current in the North Atlantic Ocean, *C. M. 1977/C:32*, 21 pp., Hydrogr. Comm., Int. Council for the Explor. of the Sea, Copenhagen, 1977.

Tenore, K., et al., Coastal upwelling in the Rias Bajas, N. W. Spain: Contrasting the benthic regimes of the rias de Arosa and de Muros, *J. Mar. Res., 40*(3), 701–772, 1982.

Tenore, K., R. Cal, R. Hanson, E. Lopez-Jamar, G. Santiago, and J. Tietjen, Coastal upwelling off the Rias Bajas, Galicia, northwest Spain, II, Benthic studies, *Rapp. P. V. Reun. Cons. Int. Explor. Mer., 183*, 91–100, 1984.

Walsh, J., and W. Esaias, Satellite detection of phytoplankton export from the Mid-Atlantic Bight during the 1979 spring bloom, *Deep Sea Res.*, in press, 1986.

Wooster, W., A. Bakun, and D. McLain, The seasonal upwelling cycle along the eastern boundary of the North Atlantic, *J. Mar. Res., 34*(2), 131–141, 1976.

L. P. Atkinson, Department of Oceanography, Old Dominion University, Norfolk, VA 23508.

J. O. Blanton, Skidaway Institute of Oceanography, Savannah, GA 31406.

S.-Y. Chao, Center for Environmental and Estuarine Studies, University of Maryland, Cambridge, MD 21613.

F. de Castillejo, Instituto Español de Oceanografía, Málaga, Spain.

C. R. McClain, Laboratory for Oceans, NASA Goddard Space Flight Center, Code 671, Greenbelt, MD 20771.

(Received November 20, 1985;
accepted January 7, 1986.)